

# Promising High Temperature Thermoelectric Performance of Alkali Metal-based Zintl phases $X_2AgY$ ( $X = Na, K$ ; $Y = Sb, Bi$ ): Insights from First-Principles Studies

Mohd Zeeshan,<sup>1</sup> Indranil Mal,<sup>1</sup> and B. K. Mani<sup>1,\*</sup>

<sup>1</sup>*Department of Physics, Indian Institute of Technology, Hauz Khas, New Delhi 110016, India*

(Dated: February 20, 2025)

In the quest for novel thermoelectric materials to harvest waste environmental heat, we investigate alkali metal-based Zintl phases  $X_2AgY$  ( $X = Na, K$ , and  $Y = Sb, Bi$ ) utilizing first-principles methods. We obtain significantly low lattice thermal conductivity values ranging  $0.9-0.5 \text{ W m}^{-1} \text{ K}^{-1}$  at 300 K, challenging established thermoelectric materials such as SnSe, PbTe,  $Bi_2Te_3$  as well as other Zintl phases. We trace such astonishingly low values to lattice anharmonicity, large phonon scattering phase space, low phonon velocities, and lifetimes. In K-based materials, the low phonon velocities are further linked to flattened phonon modes arising from the gap in the optical spectrum. Furthermore, the existence of bonding heterogeneity could hamper heat conduction in these materials. In addition, an avoided crossing in the phonon dispersions suggesting rattling behavior, observed in all materials except  $Na_2AgSb$ , suppresses the dispersion of acoustic modes, further reducing the phonon velocities. When combined with electrical transport calculations, the materials exhibit high figure of merit values at 700 K, i.e.,  $ZT \sim 2.1$  for  $Na_2AgSb$ , 1.7 for  $Na_2AgBi$ , 0.9 for  $K_2AgSb$ , and 1.0 for  $K_2AgBi$ . Our predicted  $ZT$  values are competitive with state-of-the-art thermoelectric materials such as  $Mg_3Sb_2$ ,  $ZrCoBi$ ,  $PbTe$ ,  $SnSe$ , and as well as with contemporary Zintl phases. Our findings underscore the potential of light alkali metal atoms combined with Ag-Bi/Sb type frameworks to achieve superior thermoelectric performance, paving the way for material design for specific operating conditions.

## I. INTRODUCTION

World's primary energy demand is still predominantly met by the consumption of fossils [1]. However, fossils are nonrenewable and will not last forever [2]. The current energy consumption rate and increasing population demand will likely deplete the resources faster [3]. On the other hand, the bleak efficiency of the energy produced is also concerning [4]. Almost 60% of the energy produced is lost to the environment in the form of heat [5]. This alarming rate of heat rejection to the environment could lead to climate changes. It is also well known that the combustion of fossils contributes to greenhouse gases, ultimately facilitating global warming [6]. Thus, there is a pressing need and high time to look beyond conventional power generation methods. Various clean renewable alternatives have been devised, such as solar cells [7], hydrogen storage materials [8], and many others [9]. However, these technologies are yet to find a firm footing as alternative sources of power generation. Researchers around the globe have been actively engaged in overcoming the hurdles associated with sustainable power generation.

In the same endeavor, thermoelectricity has emerged as a promising alternative for power generation [10]. The technology can harvest the environment's enormous waste heat into electricity [11]. This will eventually ease the burden on the existing resources by improving the efficiency of energy usage. Further, if scaled well, thermoelectricity could be a plausible alternative source of

power generation. Despite the stated benefits, the commercialization of these materials is hindered by their low efficiency [12]. The efficiency of thermoelectric material is based on the temperature gradient and a dimensionless quantity called the figure of merit, which is expressed as  $ZT = S^2\sigma T/(\kappa_e + \kappa_L)$ , where  $S$ ,  $\sigma$ ,  $T$ , and  $\kappa$  are the Seebeck coefficient, electrical conductivity, temperature, and thermal conductivity including electronic and lattice thermal contributions [13–15]. The electronic part ( $S$ ,  $\sigma$ , and  $\kappa_e$ ) is heavily interconnected and poses a challenge for simultaneous optimization, resulting in lower thermoelectric efficiency [16–18].

The two distinct strategies to improve the figure of merit are improving the numerator part,  $S^2\sigma$ , also called as power factor, and lowering the  $\kappa_L$  [19]. The power factor has been successfully improved using band engineering [20], optimizing carrier concentration [21], and resonant doping [22]. On the other hand, the  $\kappa_L$  is significantly lowered by adopting nanostructuring [23], introducing defects through vacancies or alloying [24], and including grain boundaries [25]. However, the two approaches often interfere, ultimately deteriorating the overall figure of merit [26]. Interestingly, many systems possess inherently low  $\kappa_L$  [27–31]. Such systems derive low  $\kappa_L$  through intrinsic rattlers, hierarchical bonding, complexed crystal structures, anharmonicity in lattice vibrations, low sound velocities, and high atomic displacements. The inherently low  $\kappa_L$ , which is nearly independent of the electronic part, allows to independently tune the electronic part, i.e., the basis of Slack's phonon-glass electron-crystal (PGEC) concept. According to the PGEC concept [32], a good thermoelectric material should possess glass like  $\kappa_L$  and crystal like electrical conductivity.

---

\* bkmani@physics.iitd.ac.in

Zintl phases, in principle, have been great contenders in recent times to follow the PGEC concept to a certain extent [33–35]. Numerous Zintl phases are reported to exhibit good thermoelectric properties based on inherently low  $\kappa_L$  and reasonable power factor. For instance,  $\text{Yb}_{14}\text{MnSb}_{11}$  [36] ( $ZT \sim 1$  at 1200 K),  $\text{Ca}_5\text{Al}_2\text{Sb}_6$  [37] ( $ZT > 0.6$  at 1000 K),  $\text{Sr}_3\text{AlSb}_3$  [38] ( $ZT \sim 0.3$  at 600 K), and  $\text{BaCuSb}$  [39] ( $ZT \sim 0.48$  at 1010 K) derive good figure of merit values based on their inherently low  $\kappa_L$ . It is important to note that Zintl phases cover extensively a vast range of systems. Compounds fulfilling the criterion of electropositive ions donating electrons to the otherwise anionic framework lie under the umbrella of Zintl phases [40]. However, not all Zintl phases could be potential thermoelectric candidates. Since the Zintl family is large and continuously growing, identifying the potential thermoelectric Zintl phases could significantly contribute to the ongoing research.

First-principles simulations can greatly facilitate the cause and provide a roadmap for experimental investigations. For instance, in Ref. [41], authors investigated that bonding hierarchy led to high thermoelectric performance in Zintl phase  $\text{BaAu}_2\text{P}_4$ . In another study, Wang *et al.* [42] investigated nine Zintl phases and found a high figure of merit for  $\text{SrAgSb}$  ( $ZT \sim 0.94$  at 400 K), based on enhanced phonon scattering due to softening of acoustic phonons. Very recently, Wei *et al.* [43] reported a high figure of merit for Zintl compound  $\text{KSrBi}$  ( $ZT \sim 2.8$  at 800 K). This was attributed to the low  $\kappa_L$  arising from rattling vibrations and occupied antibonding states. Motivated by such recent findings, we decided to computationally explore unreported Zintl phases for thermoelectrics.

In this work, we use first-principles based methods to systematically investigate the electronic and thermal transport properties of the alkali metal-based family of Zintl phases  $\text{X}_2\text{AgY}$  ( $\text{X} = \text{Na}, \text{K}$ , and  $\text{Y} = \text{Sb}, \text{Bi}$ ). We report significantly low lattice thermal conductivity values competing well with established thermoelectric materials such as  $\text{SnSe}$ ,  $\text{PbTe}$ , and  $\text{Bi}_2\text{Te}_3$ . To account for such low values, we investigate different aspects of thermal transport, such as phonon scattering phase space, velocities, lifetimes, and lattice anharmonicity. In all systems except  $\text{Na}_2\text{AgSb}$ , we find an avoided crossing characteristic of rattling behavior associated with suppressing the dispersion of acoustic modes. Such a phenomenon leads to reduced slopes and low phonon velocities. Particularly in K-based materials, we find gap in optical modes, which often results in the flattening of phonon modes. Furthermore, we obtain bonding heterogeneity, which is disruptive to thermal conductivity. Combining such compelling thermal transport results with electrical ones, we further report tremendous figure of merit values for  $\text{Na}_2\text{AgSb}$  and  $\text{Na}_2\text{AgBi}$ . Our study signifies the microscopic origin of low lattice thermal conductivity values and regulation of carrier engineering in optimizing thermoelectric materials.

The paper is arranged as follows: In Sec. II, we briefly

provide the computational methods used for performing our simulations. In Sec. III, we elucidate our results on structural optimization, thermal transport, and electrical transport properties. In Sec. IV, we discuss the aspects pertaining to the experimental realization of proposed properties and also highlight the prospects of the work. To conclude, a summary of the work is presented in Sec. V of the paper.

## II. COMPUTATIONAL METHODS

First-principles simulations based on density functional theory (DFT) are performed using Vienna *ab initio* simulation package (VASP) [44, 45]. The interactions between core and valence electrons are accounted using projector-augmented wave pseudopotentials. The exchange-correlations among electrons are treated using the generalized gradient approximation (GGA) based Perdew-Burke-Ernzerhof (PBE) pseudopotential [46]. The cutoff energy of 500 eV is used for the plane-waves for all four systems. The Monkhorst-Pack scheme is used for Brillouin zone integration. The ground state structural parameters are obtained using a  $k$  grid of  $11 \times 11 \times 11$ , whereas a denser grid of  $21 \times 21 \times 21$  is used for self-consistent energy calculations, ensuring sufficient accuracy for transport properties. The total energy and forces convergence criteria are set as  $10^{-8}$  eV and  $10^{-7}$  eV/Å, respectively.

The electronic structure is calculated using the modified Becke-Johnson (mBJ) potential [47]. In addition, relativistic effects are included to account for the contribution of heavy atoms in the proposed systems. We employed TB-LMTO-ASA code [48] to investigate the crystal orbital Hamilton population (COHP) and bonding characteristics. Based on the obtained electronic structure, we have calculated the electrical transport properties using the AMSET code [49]. We have considered three scattering mechanisms as implemented in the code, viz. acoustic deformation potential, ionized impurity, and polar optical phonon. The net scattering rates are evaluated based on Matthiessen's rule [50]

$$\frac{1}{\tau_e} = \frac{1}{\tau_{\text{ADP}}} + \frac{1}{\tau_{\text{IMP}}} + \frac{1}{\tau_{\text{POP}}} \quad (1)$$

The components of scattering rates are obtained as per the Fermi's golden rule [51]

$$\tilde{\tau}_{n\mathbf{k} \rightarrow m\mathbf{k}+q}^{-1} = \frac{2\pi}{\hbar} |g_{nm}(\mathbf{k}, \mathbf{q})|^2 \delta(\epsilon_{n\mathbf{k}} - \epsilon_{m\mathbf{k}+q}) \quad (2)$$

where  $n\mathbf{k}$  represent the initial wave vector,  $m\mathbf{k} + \mathbf{q}$  is the final waver vector,  $\hbar$  is the reduced Planck's constant,  $\delta$  is the Dirac delta function,  $\epsilon$  is the electron energy, and  $g$  is the electron-phonon coupling matrix element. The input parameters required for calculated scattering mechanisms, such as elastic and dielectric constants, deformation potential, and polar optical phonon frequency, are

extracted using first-principles simulations, density functional perturbation theory, and finite differences method. The electrical transport coefficients are well tested in terms of the interpolation factor, which converges well with a value of 5.

A supercell of  $2 \times 2 \times 2$  size containing 128 atoms is used for generating the force constants by finite displacement method along with  $\Gamma$ -centered  $k$  mesh of  $2 \times 2 \times 2$ . The atomic displacements of  $0.01 \text{ \AA}$  and  $0.03 \text{ \AA}$  are used for second- and third-order force constants, respectively. The phonon dispersion curves are obtained using the Phonopy [52] code by solving the expression

$$\sum_{\beta\tau'} D_{\tau\tau'}^{\alpha\beta}(\mathbf{q})\gamma_{\mathbf{q}j}^{\beta\tau'} = \omega_{\mathbf{q}j}^2\gamma_{\mathbf{q}j}^{\alpha\tau}. \quad (3)$$

where the indices  $\tau, \tau'$  represent the atoms,  $\alpha, \beta$  are the Cartesian coordinates,  $\mathbf{q}$  is a wave vector,  $j$  is a band index,  $D(\mathbf{q})$  is the dynamical matrix,  $\omega$  is the corresponding phonon frequency, and  $\gamma$  is the polarization vector. To compute the Grüneisen parameter, the phonon calculations are performed by scaling the unit-cell volume by  $\pm 2\%$ .

The lattice thermal conductivity is determined by solving the Boltzmann transport equation for phonons within the single-mode relaxation time approximation (RTA) using the Phono3py [53] code. The intrinsic values are obtained through phonon lifetimes  $\tau_\lambda$ , group velocities  $\mathbf{v}_\lambda$ , and mode heat capacities  $C'_\lambda$ , according to the relation

$$\kappa_L = \frac{1}{NV} \sum_{\lambda} C'_\lambda \mathbf{v}_\lambda \otimes \mathbf{v}_\lambda \tau_\lambda \quad (4)$$

where  $N$  represents the number of unit-cells of the crystal and  $V$  is the volume of the unit cell. The lattice thermal conductivity is well converged in terms of cutoff pair distance ( $5 \text{ \AA}$ ) and  $q$ -grid ( $17 \times 17 \times 17 q$ ). The lifetime of phonons is determined from third-order force constants, which accounts for phonon-phonon scattering. To account for three-phonon scattering processes, we calculated phase space using ShengBTE [54] code.

### III. RESULTS

#### A. Structural Optimization

$\text{Na}_2\text{AgSb}$  crystallizes in orthorhombic  $Cmcm$  symmetry [55], while  $\text{Na}_2\text{AgBi}$  [56] is predicted to be thermodynamically stable in the same symmetry. The K-atom based systems  $\text{K}_2\text{AgSb}$  and  $\text{K}_2\text{AgBi}$  adopts orthorhombic  $C222_1$  structure [57]. The crystal structure in two symmetries,  $Cmcm$  and  $C222_1$ , bears a striking resemblance and looks fairly identical. The only notable distinction is that the atomic positions of Na/K and Ag atoms are marginally off-centered along  $c$ - and  $a$ -axis, respectively, as can be noted from structural parameters

Table I. Calculated lattice constants and band gaps. The experimental values provided in parentheses for  $\text{Na}_2\text{AgSb}$  and  $\text{K}_2\text{AgSb/Bi}$  are from the Ref. [55] and [57], respectively.

System	a (Å)	b (Å)	c (Å)	$E_g$ (eV)
$\text{Na}_2\text{AgSb}$	9.34 (9.29)	7.90 (7.90)	5.82 (5.77)	1.36
$\text{Na}_2\text{AgBi}$	9.51	8.04	5.87	0.87
$\text{K}_2\text{AgSb}$	10.61 (10.44)	8.36 (8.29)	6.36 (6.28)	1.87
$\text{K}_2\text{AgBi}$	10.79 (10.56)	8.48 (8.38)	6.46 (6.33)	0.99

in Supplemental Material [58]. Thus, the crystal structure of all four systems can be conveniently represented by the structure shown in Fig. 1(a). The structure can be visualized as the infinite zigzag chains of Ag-Sb/Bi well separated from parallel chains by Na/K atoms along  $a$ -axis. Nevertheless, to ensure the accuracy of our simulations, we optimized the four systems in their respective symmetries. Our calculated lattice parameters are in agreement with experimental values ( $\pm 2\%$ ), as evident from Table I. Using these optimized parameters, we calculated the electronic structure, as discussed next.

#### B. Electronic Structure

Understanding electronic structure is quintessential for knowing the thermoelectric performance of a material. The electronic structure calculated using standard DFT functionals like PBE is known to underestimate the band gap. Therefore, we have employed mBJ potential in our simulations. The mBJ is known to provide band gaps with accuracy similar to hybrid functionals; however, it is less computationally expensive. In addition, to account for the heavier atoms, we have also incorporated spin-orbit coupling in our simulations. Our calculated electronic structures of four systems are depicted in Fig. 1. All materials are semiconducting in nature, bearing band gap in the range (0.8–1.8 eV). The values seem sufficient to avoid any bipolar conduction, which could be beneficial for thermoelectric materials. The nature of band gap is direct for  $\text{Na}_2\text{AgSb}$ ,  $\text{Na}_2\text{AgBi}$ , and  $\text{K}_2\text{AgSb}$ , where valence band maximum (VBM) and conduction band minimum (CBM) lies along  $\Gamma$ -point. For  $\text{K}_2\text{AgBi}$ , the VBM is off-gamma at  $(-0.381135 \ 0.488430 \ 0.43478)$   $k$ -point along T-X direction, whereas CBM lies along  $\Gamma$ .

The band curvature and slope provide insight into the behavior of  $S$  and  $\sigma$ . The steep dispersed bands have lighter effective mass of charge carriers, which contributes to electrical conductivity, whereas the flat bands have higher effective mass beneficial for the Seebeck coefficient. All the systems have more dispersed bands in the conduction band region, which suggests high  $\sigma$  for  $n$ -type systems. On the other hand, the valence band region displays a mix of mostly flat bands close to the Fermi level, followed by some dispersed bands. Thus,  $p$ -type systems

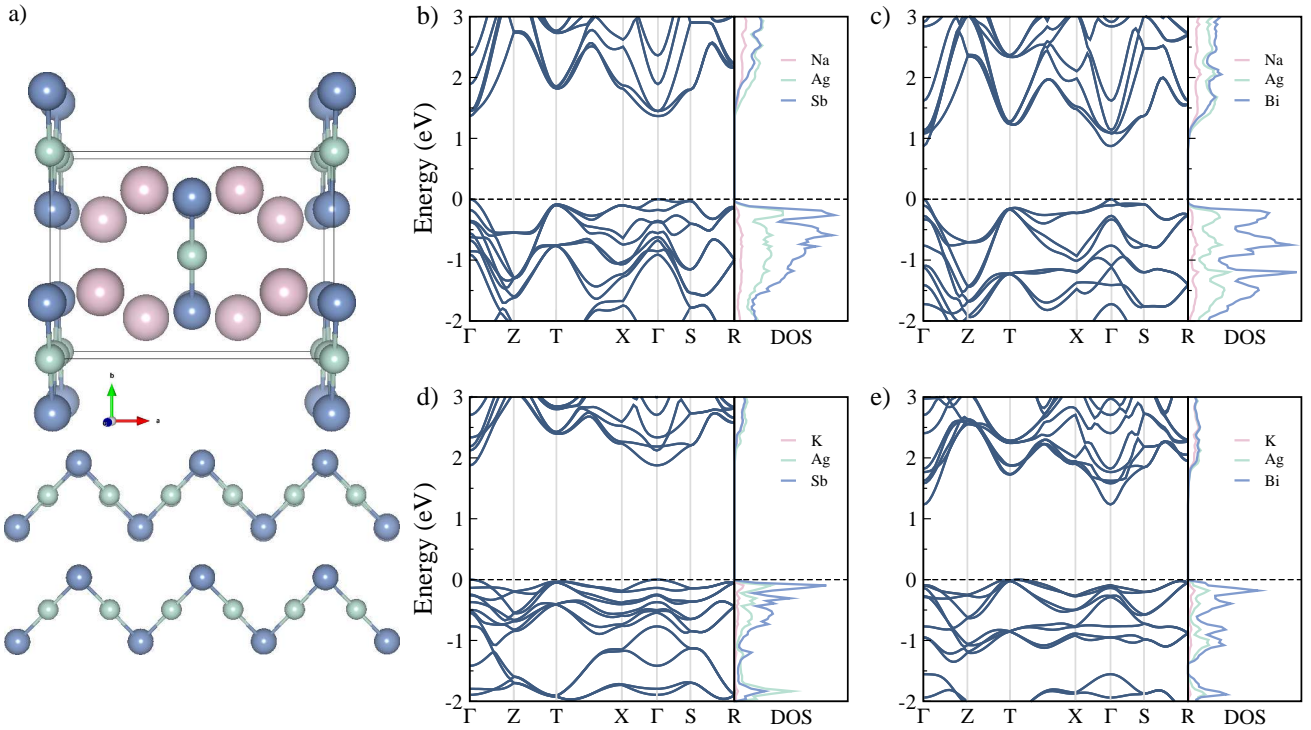


Figure 1. (a) Crystal structure of  $X_2AgY$  ( $X = Na/K$ ,  $Y = Sb/Bi$ ) in orthorhombic  $Cmc$  symmetry and the zigzag alignment of Ag-Sb/Bi, (b), (c), (d), and (e) are electronic structures of  $Na_2AgSb$ ,  $Na_2AgBi$ ,  $K_2AgSb$ , and  $K_2AgBi$ , respectively. The density of states is shown in arbitrary units.

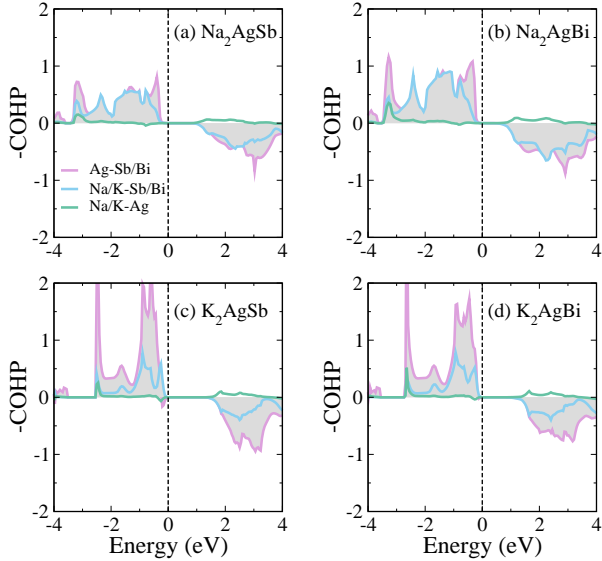


Figure 2. Crystal orbital Hamiltonian population of (a)  $Na_2AgSb$ , (b)  $Na_2AgBi$ , (c)  $K_2AgSb$ , and (d)  $K_2AgBi$ .

are likely to have high Seebeck coefficient. The presence of flat bands along with dispersed ones also hints at larger power factor for  $p$ -type systems.

The density of states show the dominant contribution of Sb/Bi in valence band maxima in all the systems, whereas the conduction band minima is populated

by the zigzag alignment of Ag-Sb/Bi in  $Na_2AgSb/Bi$ . The conduction band minima in K-based compositions, i.e.,  $K_2AgSb/Bi$ , is almost equally contributed by all the atoms.

To gain insight into bonding characteristics, we further performed COHP analysis, Fig. 2. This helps in predicting the bonding nature by allocating the electronic energy into individual orbital interaction pairs. The positive and negative COHP values represent the bonding and antibonding states, respectively. No antibonding states are observed below the Fermi level for the plausible interactions (Na/K-Ag, Na/K-Sb/Bi, and Ag-Sb/Bi). Across the materials, the interactions between alkali and silver atoms (Na/K-Ag) are negligible. The interactions between Ag-Sb/Bi are dominant, followed by Na/K-Sb interactions. This fits well with the classical description of Zintl phases [59], where Na/K atoms are loosely bounded to the Ag-Sb/Bi framework. The interactions between the Ag-Sb/Bi and Na-Sb/Bi are pretty similar in  $Na_2AgSb/Bi$ . On the other hand, the interactions between the Ag-Sb/Bi are more pronounced in comparison to K-Sb/Bi in K-based materials. This reasonable disparity suggests the more bonding heterogeneity in  $K_2AgSb/Bi$ , detrimental to lattice thermal conductivity.

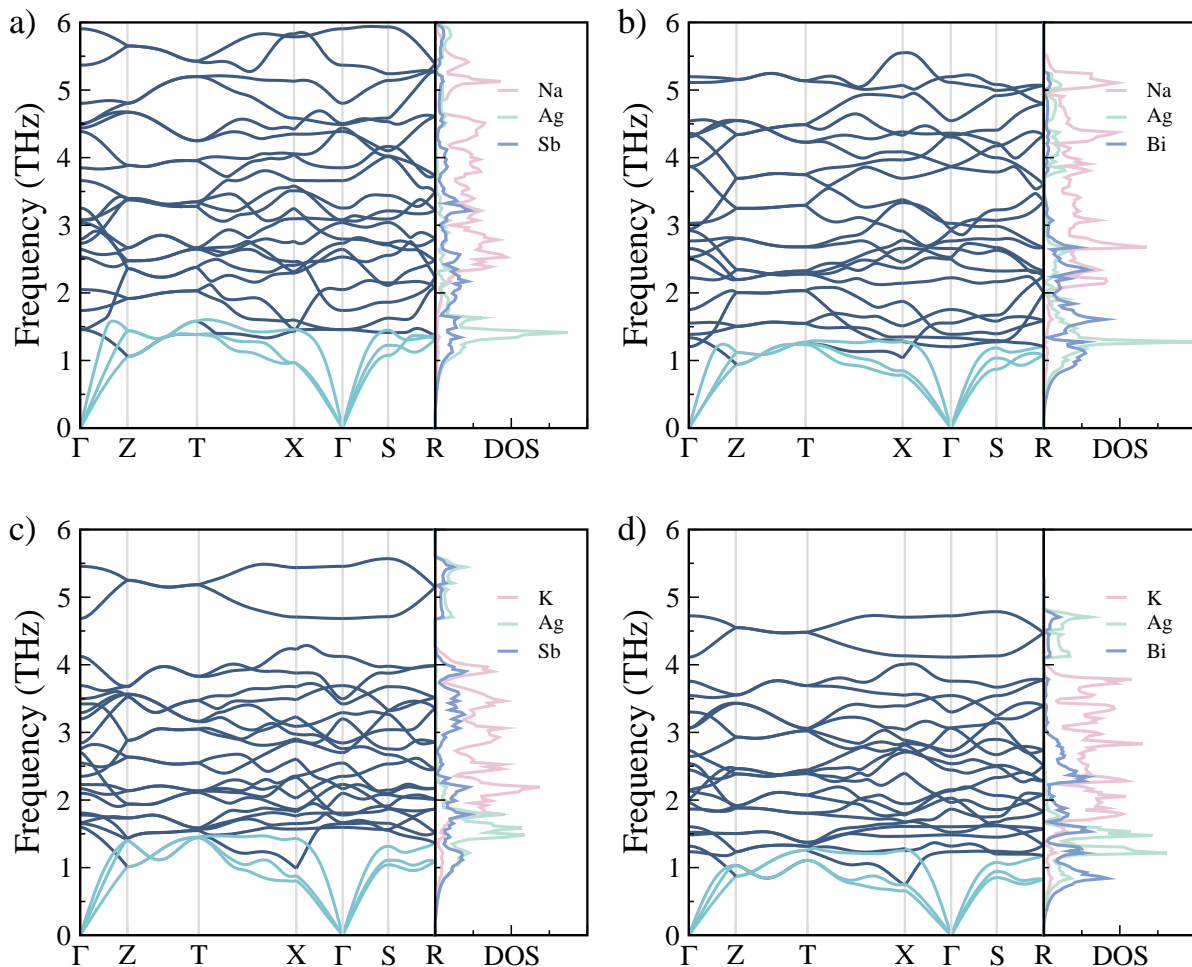


Figure 3. Phonon band structures and partial density of states of (a)  $\text{Na}_2\text{AgSb}$ , (b)  $\text{Na}_2\text{AgBi}$ , (c)  $\text{K}_2\text{AgSb}$ , and (d)  $\text{K}_2\text{AgBi}$ . The density of states is shown in arbitrary units.

### C. Phonons

Now, we are moving on to phonon dispersion curves, which play a pivotal role in transport properties. The phonon dispersion curves and density of states are shown in Fig. 3. The primitive crystal structure has 8 atoms, resulting in 24 phonon bands at each wave vector. The dynamical stability of a crystal structure is crucial for accurately predicting its properties. No imaginary frequencies in the phonon dispersions suggest that the crystal structure can sustain lattice vibrations and is unlikely to undergo a phase transition or structural distortions. The phonon dispersions range  $\sim 5.9$  THz in  $\text{Na}_2\text{AgSb}$ , which flattens to  $\sim 4.8$  THz in  $\text{K}_2\text{AgBi}$ . Such low frequencies of phonon modes are likely to have low group velocities,  $\nu_g = d\omega/dq$ , catering to low  $\kappa_L$ . The steep acoustic modes flatten out between  $\sim 1$ - $1.5$  THz and thereafter followed by relatively flat low-lying optical modes. It can also be seen that one of the optical modes coincides with acoustic modes.

It is interesting to note the band gap in high frequency optical modes in  $\text{K}_2\text{AgSb}$  and  $\text{K}_2\text{AgBi}$  at  $\sim 4.3$

and  $\sim 4.0$  THz, respectively. Such band gaps are associated with the flattening of phonon modes, resulting in low group velocities and thereby low  $\kappa_L$  [60]. Further, there is an avoided crossing between acoustic and optical modes along the  $\Gamma$ -S-R direction ( $\sim 1.1$  THz) in all the systems except  $\text{Na}_2\text{AgSb}$ . This avoided crossing is characteristic of rattling behavior in the system. Such avoided crossings suppress the dispersion of acoustic modes, leading to reduced slopes and lower phonon group velocities, conducive to low  $\kappa_L$  [61].

The phonon density of states help get an insight into the atomic contribution towards various phonon modes. The acoustic modes primarily responsible for the heat conduction in the lattice are contributed mainly by Ag in  $\text{Na}_2\text{AgSb}$ , with some contribution from Sb atoms. In the case of  $\text{K}_2\text{AgSb}$ , the Ag and Sb contribute almost equally to the acoustic modes, whereas Bi dominates the acoustic region in  $\text{Na}_2\text{AgBi}$  and  $\text{K}_2\text{AgBi}$ . The mid-frequency phonons see a dominant contribution from the alkali atoms Na/K, whereas the high frequency optical modes are contributed by the lighter Na atoms in  $\text{Na}_2\text{AgSb}$  and  $\text{Na}_2\text{AgBi}$ . Surprisingly, the high frequency

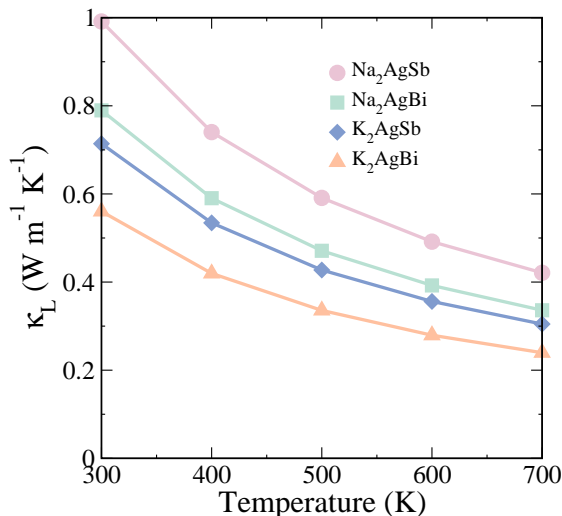


Figure 4. Average lattice thermal conductivity as a function of temperature for  $\text{Na}_2\text{AgSb}$ ,  $\text{Na}_2\text{AgBi}$ ,  $\text{K}_2\text{AgSb}$ , and  $\text{K}_2\text{AgBi}$ .

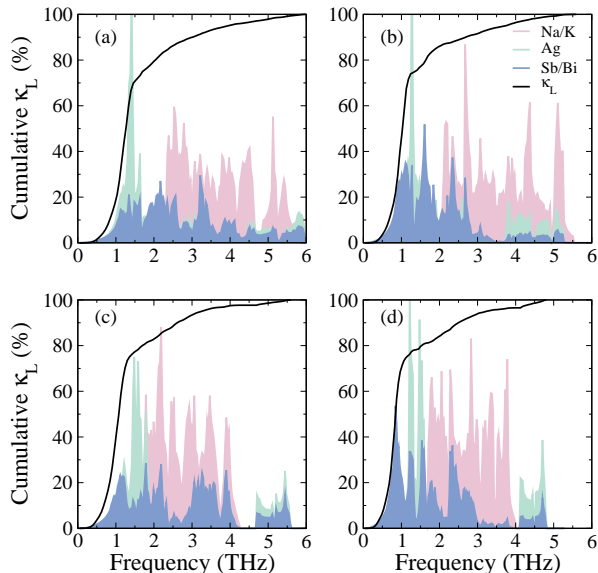


Figure 5. Cumulative lattice thermal conductivity in % as a function of phonon frequency at 300 K for (a)  $\text{Na}_2\text{AgSb}$ , (b)  $\text{Na}_2\text{AgBi}$ , (c)  $\text{K}_2\text{AgSb}$ , and (d)  $\text{K}_2\text{AgBi}$ . The phonon density of states in arbitrary units are overlaid.

optical modes above the band gap are contributed by Ag and Sb/Bi in K-based systems  $\text{K}_2\text{AgSb}$  and  $\text{K}_2\text{AgBi}$  despite the lighter mass of K atoms, which could be a subject of further study. Next, we discuss the trend of  $\kappa_L$  for different systems.

#### D. Lattice Thermal Conductivity

Figure 4 illustrates the trend of average  $\kappa_L$  as a function of temperature for different systems. The average

values are obtained using the arithmetic mean along different crystallographic directions. Our calculated values can be seen as an upper bound, considering the RTA method takes into account only the three-phonon scattering processes. It has been demonstrated that the four-phonon scattering process further reduces the  $\kappa_L$  [62–64]. The  $\kappa_L$  values are also subject to the real material, which may have defects, grain boundaries, and other imperfections. All these said factors are likely to lower the  $\kappa_L$  further.

For all the systems, a decreasing trend of  $\kappa_L$  with temperature can be noticed. The behavior is consistent with the more pronounced phonon-phonon scattering at higher temperatures. The lower values at high temperature signify the efficient thermoelectric performance at high temperatures. Across the materials,  $\text{Na}_2\text{AgSb}$  exhibit the highest  $\kappa_L$  values starting at  $0.9 \text{ W m}^{-1} \text{ K}^{-1}$  at 300 K and decreasing to  $0.4 \text{ W m}^{-1} \text{ K}^{-1}$  at 700 K. The  $\text{Na}_2\text{AgBi}$  and  $\text{K}_2\text{AgSb}$  show intermediate  $\kappa_L$  values both starting at around  $0.7 \text{ W m}^{-1} \text{ K}^{-1}$  at 300 K and falling to approximately  $0.3 \text{ W m}^{-1} \text{ K}^{-1}$  at 700 K. The standout material is  $\text{K}_2\text{AgBi}$  exhibiting strikingly low  $\kappa_L$  values ranging  $0.56\text{--}0.23 \text{ W m}^{-1} \text{ K}^{-1}$  in the temperature window 300–700 K. Our measured  $\kappa_L$  values are significantly low and compete well with established thermoelectric materials SnSe [65] ( $\kappa_L \sim 0.47 \text{ W m}^{-1} \text{ K}^{-1}$  at 300 K), PbTe [66] ( $\kappa_L \sim 2.0 \text{ W m}^{-1} \text{ K}^{-1}$  at 300 K),  $\text{Bi}_2\text{Te}_3$  [67] ( $\kappa_L \sim 1.6 \text{ W m}^{-1} \text{ K}^{-1}$  at 300 K), and also with other low  $\kappa_L$  reported Zintl phases [37–39].

To gain insight into such astonishingly low  $\kappa_L$  values, we first understand the individual atomic and phonon modes contribution to  $\kappa_L$ . This helps optimize the material’s performance by possibly reducing the  $\kappa_L$  through desirable structural modifications. As discernible from Fig. 5, the cumulative nature of the curves shows that approximately 80% contribution to  $\kappa_L$  comes from acoustic and low-lying optical modes below 2 THz. Notably, the acoustic modes alone contribute  $\sim 71$  to  $77\%$  towards  $\kappa_L$  on going from  $\text{Na}_2\text{AgSb}$  to  $\text{K}_2\text{AgBi}$ . There is a marked decrease in contributions from high frequency optical modes. Now, these primary heat carrying acoustic modes are contributed majorly by Ag in  $\text{Na}_2\text{AgSb}$ , Ag and Bi in  $\text{Na}_2\text{AgBi}$ , Ag and Sb in  $\text{K}_2\text{AgSb}$ , and Bi in  $\text{K}_2\text{AgBi}$ . Thus, any attempt to further reduce  $\kappa_L$  should aim to alloy at these respected sites.

Now, we move to another critical parameter in understanding the  $\kappa_L$ , i.e., phonon group velocity,  $\nu_g$ . The group velocity typically decreases with increasing phonon frequency, as discernible from Fig. 6(a). This could be attributed to the more scattering tendency of higher frequency phonons, which hinders energy transport. It can also be observed that group velocity decreases with increasing atomic mass on going from  $\text{Na}_2\text{AgSb}$  to  $\text{K}_2\text{AgBi}$ . This is because the heavier atoms are likely to undergo smaller vibrations. The low group velocities in  $\text{K}_2\text{AgSb}$  and  $\text{K}_2\text{AgBi}$ , as discussed earlier, can also be attributed to the gap in phonon modes, associated with the flattening of phonon modes and resulting in low group veloc-

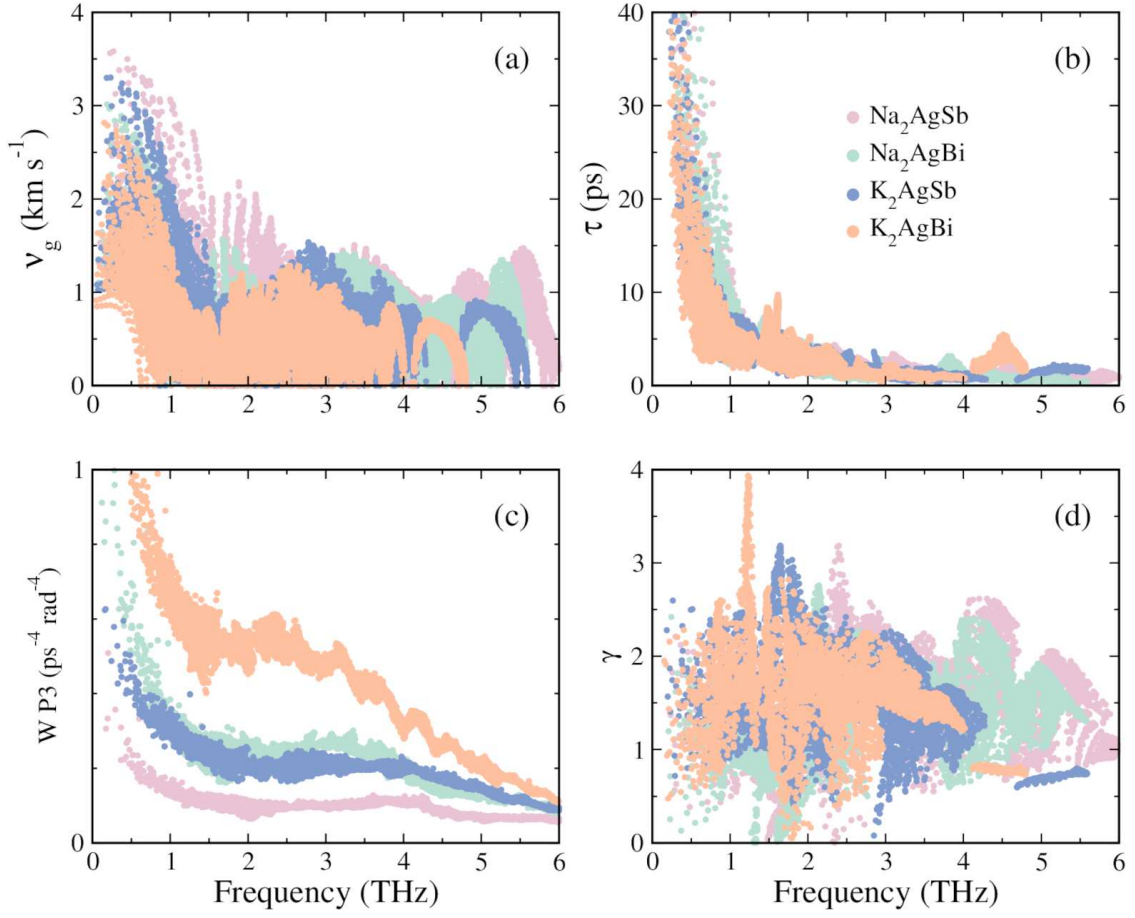


Figure 6. (a) Phonon group velocities, (b) lifetime, (c) weighted scattering phase space, and (d) Grüneisen parameter as a function of frequency for Na<sub>2</sub>AgSb, Na<sub>2</sub>AgBi, K<sub>2</sub>AgSb, and K<sub>2</sub>AgBi.

ities. The majority of the acoustic modes (up to  $\sim 1.6$  THz) possess low group velocities ( $\nu_g < 1.5 \text{ km s}^{-1}$ ). As already seen, the acoustic modes contributing most to the  $\kappa_L$ , the low group velocities of acoustic modes could be valuable. On the other hand, the bulk mid-frequency phonons exhibit  $\nu_g < 1 \text{ km s}^{-1}$ , whereas the most high frequency optical modes exhibit even lesser  $\nu_g$ .

The sound velocities obtained from the slopes of the acoustic modes allow a better comparative analysis of our results with other reported works. The average values are obtained using the expression  $\frac{3}{\nu_s^3} = \frac{1}{\nu_l^3} + \frac{2}{\nu_t^3}$ , where  $\nu_l$  and  $\nu_t$  are the longitudinal and transverse sound velocities, respectively. Our calculated sound velocities for Na<sub>2</sub>AgSb, Na<sub>2</sub>AgBi, K<sub>2</sub>AgSb, and K<sub>2</sub>AgBi are 2.2, 1.9, 2.0, and 1.7  $\text{km s}^{-1}$ , respectively. Such remarkably low sound velocities are comparable to standard thermoelectric materials such as SnSe [65] (3.1  $\text{km s}^{-1}$ ), PbTe [66] (1.7  $\text{km s}^{-1}$ ), and Bi<sub>2</sub>Te<sub>3</sub> [67] (1.5  $\text{km s}^{-1}$ ).

It is instructive to examine the phonon lifetimes as they are linearly proportional to the  $\kappa_L$  by Eqn. 4. The phonon lifetimes as extracted using three-phonon scattering processes are depicted in Fig. 6(b). The lifetime of acoustic modes ( $\sim 1$ -1.5 THz) is nearly one order

higher than the optical modes, indicative of the dominant contribution of acoustic modes to  $\kappa_L$ . The high frequency optical phonon modes ( $> 3$  THz) tend to scatter readily due to interactions such as Umklapp processes, which result in smaller lifetimes. Evidently, the lifetime of Na<sub>2</sub>AgSb and Na<sub>2</sub>AgBi across the spectrum are higher in comparison to K<sub>2</sub>AgSb and K<sub>2</sub>AgBi, partially accounting for their higher  $\kappa_L$ . It is obvious to note that Na<sub>2</sub>AgBi and K<sub>2</sub>AgBi exhibit lower frequencies in the optical phonon branches compared to their Sb counterparts, suggesting increased phonon-phonon scattering. Further, the K-based systems (K<sub>2</sub>AgSb and K<sub>2</sub>AgBi) shows lower phonon lifetimes than their Na-based counterparts. Thus, it can be surmised that substituting Na/Sb with K/Bi may reduce the phonon lifetime and  $\kappa_L$ . The majority of phonon modes have lifetimes of less than 10 ps, which suggests anharmonicity and strong phonon-phonon scatterings. The average lifetimes across the systems are less than  $\sim 3$  ps, fairly consistent with SnSe [68] (3.2 ps at 300 K).

To delve deeper into understanding the trend of  $\kappa_L$ , we next investigate the phase space, which describes the available states for phonon scattering, weighted according to interaction probabilities. A large phase space is

an indication of more phonon scattering events. As discernible from Fig. 6(c),  $K_2AgBi$  has the largest phase space among the materials. Indeed, the phase space for  $K_2AgBi$  is nearly double the size of  $Na_2AgBi$  and  $K_2AgSb$ , and almost four times that of  $Na_2AgSb$ . Verily, this accounts for the lowest  $\kappa_L$  in  $K_2AgBi$ . The phase space trend also highlights how substituting heavier atom (Na/Sb by K/Bi) influences scattering behavior. The large phase space of  $Na_2AgBi$  ( $K_2AgBi$ ) in comparison to  $Na_2AgSb$  ( $K_2AgSb$ ) suggests that heavier atoms shift phase space distribution. This very fact can be leveraged in material design to tune the desirable properties through phonon scattering control. The large phase space values also indicate the strong anharmonicity in the systems.

To quantify the same, we evaluated the Grüneisen parameter ( $\gamma$ ), which is a measure of anharmonicity in the crystal lattice. As discernible from Fig. 6(d), the majority of phonon modes have  $\gamma$  greater than unity. The average values of  $\gamma$  are 1.53, 1.40, 1.48, and 1.57 for  $Na_2AgSb$ ,  $Na_2AgBi$ ,  $K_2AgSb$ , and  $K_2AgBi$ , respectively. These values align closely with those reported for materials exhibiting low  $\kappa_L$ , where significant anharmonicity dominates the lattice vibrations. For instance, SnSe ( $\gamma \sim 1.7$ ),  $Bi_2Te_3$  ( $\gamma \sim 1.5$ ), and PbTe ( $\gamma \sim 1.4$ ) exhibit comparable values, highlighting the strong anharmonicity in these systems. Meanwhile, the largest  $\gamma$  for  $K_2AgBi$  can be attributed to large values of  $\gamma$  in the acoustic region. The  $\gamma$  in the acoustic region reaches  $\sim 4$  for  $K_2AgBi$ , whereas other materials have a maximum  $\gamma < 2.6$ . The large  $\gamma$  of  $K_2AgBi$  also justifies its low  $\kappa_L$  in comparison to other materials.

The promising thermal transport warrants further assessment of electrical transport properties to obtain thermoelectric efficiency. In the following section, we evaluate and understand the electrical transport coefficients.

### E. Electrical Transport Properties

In this section, we will discuss the temperature and carrier-concentration dependent electrical transport properties obtained by solving the Boltzmann transport equation using inputs from density functional theory. Given the fact that Zintl phases have a natural tendency to form  $p$ -type compositions [69, 70] and a glimpse of better  $p$ -type transport properties from the electronic structure discussion, we emphasize here our results for  $p$ -type systems. Interested readers are directed to Supplemental Material [58] for the  $n$ -type systems. We take the liberty of discussing our results at 300, 500, and as high as 700 K, based on the synthesis temperature of 973 K ( $Na_2AgSb$ ) and 873 K ( $K_2AgSb$  and  $K_2AgBi$ ). Figure 7 shows our calculated results for the figure of merit at different temperatures and carrier concentrations.

As discernible from the figure, the thermoelectric figure of merit increases with temperature for the given carrier concentration range of  $10^{18}$  to  $10^{21}$   $cm^{-3}$ . Our predicted

maximum values of the figure of merit are,  $ZT \sim 2.1$ , 1.7, 0.9, and 1.0 at 700 K for  $Na_2AgSb$ ,  $Na_2AgBi$ ,  $K_2AgSb$ , and  $K_2AgBi$ , respectively, for carrier concentration in the range of  $10^{20}$   $cm^{-3}$ . The comparatively lower values for  $K_2AgSb$  and  $K_2AgBi$  highlight the influence of Na substitution with K on thermoelectric performance. Nevertheless, these values are substantially high and compete well with contemporary Zintl phases, e.g.,  $Mg_3Sb_2$  [71] ( $ZT \sim 1.5$  at 716 K),  $Yb_{10}MgSb_9$  [72] ( $ZT \sim 1.0$  at 873 K),  $NaCdSb$  [73] ( $ZT \sim 1.3$  at 673 K), and  $BaCuSb$  [39] ( $ZT \sim 0.4$  at 1010 K). Besides, the predicted values also resonate well with other state-of-the-art materials such as half-Heusler alloys ( $ZT \sim 1.4$  and 1.5 at 973 K for  $ZrCoBi$  [74] and  $TaFeSb$  [75], respectively), skutterudite  $CoSb_3$  [76] ( $ZT \sim 1.7$  at 823 K),  $PbTe$ - $SrTe$  [77] ( $ZT \sim 2.5$  at 923 K), and  $SnSe$  [65] ( $ZT \sim 2.6$  at 913 K).

Having said that, the optimal carrier concentrations are slightly on the higher side for a doped semiconductor. Nonetheless, considering the experimental challenges, one can target slightly lower carrier concentrations ( $\sim 10^{19}$   $cm^{-3}$ ) to breach the figure of merit of unity for Na-based compounds. It is noteworthy that despite having the lowest  $\kappa_L$ , the  $ZT$  of  $K_2AgBi$  is also the lowest. To dissect this, we now break down into individual components of electrical transport. The coefficients  $S$ ,  $\sigma$ ,  $\kappa_e$ , and  $S^2\sigma$  for the optimal carrier concentrations with respect to temperature are shown in Fig. 8. The Seebeck coefficient represents the change in voltage with respect to temperature and is generally expressed as

$$S = \frac{8\pi^2 k_B^2}{3eh^2} m_{DOS}^* T \left( \frac{\pi}{3n} \right)^{2/3} \quad (5)$$

where  $k_B$ ,  $e$ ,  $h$ ,  $n$ ,  $m_{DOS}^*$ , represents the Boltzmann constant, elementary charge, Planck's constant, carrier concentration, and effective mass of charge carrier, respectively. The Eq. 5 shows the contradictory dependence of  $S$  on carrier concentration and temperature. We have observed a similar trend for the calculated values. As discernible from Fig. 8(a), the  $S$  increases with temperature for all the systems. Further, beyond 300 K, the  $S$  gradually picks up for  $Na_2AgSb/Bi$  in comparison to  $K_2AgSb/Bi$  on account of slightly lower optimal carrier concentrations.  $Na_2AgBi$  exhibits the highest value ( $\sim 296$   $\mu V K^{-1}$ ), closely followed by  $Na_2AgSb$ .

The electrical conductivity reflects the ease of carrier transport in a material and is expressed as  $\sigma = ne\mu$ , where  $n$  is the carrier concentration,  $e$  is the elementary charge, and  $\mu$  is the carrier mobility.  $Na_2AgSb$  and  $Na_2AgBi$  exhibit the highest conductivity values, with  $Na_2AgSb$  slightly outperforming  $Na_2AgBi$ , Fig. 8(b). Surprisingly, the  $\sigma$  values for  $K_2AgSb/Bi$  are approximately half in comparison to  $Na_2AgSb/Bi$ . The  $\sigma$  of a semiconductor is known to increase with temperature and carrier concentration. However, for degenerate semiconductors, the  $\sigma$  decreases with temperature, as observed in the present case. This decreasing behavior can be attributed to increased carrier scattering at

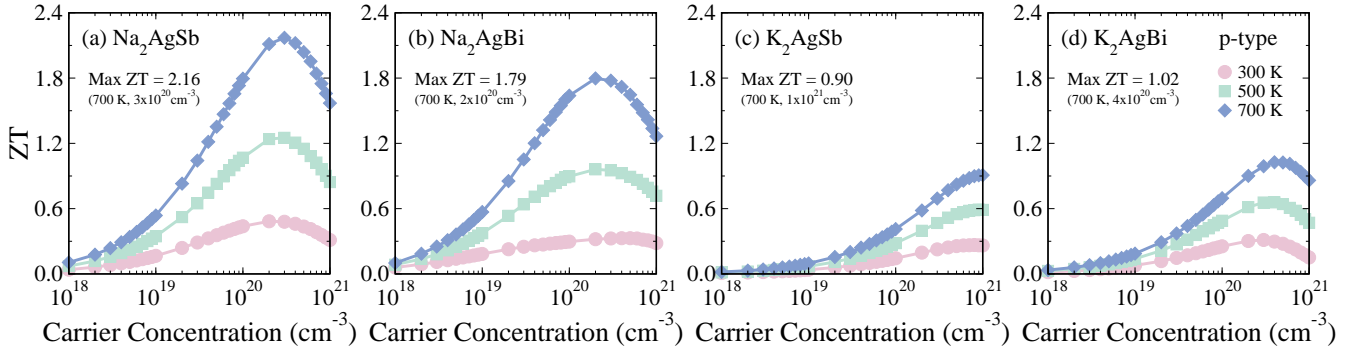


Figure 7. Thermoelectric figure of merit as a function of temperature at various carrier concentrations of  $p$ -type (a)  $\text{Na}_2\text{AgSb}$ , (b)  $\text{Na}_2\text{AgBi}$ , (c)  $\text{K}_2\text{AgSb}$ , and (d)  $\text{K}_2\text{AgBi}$ .

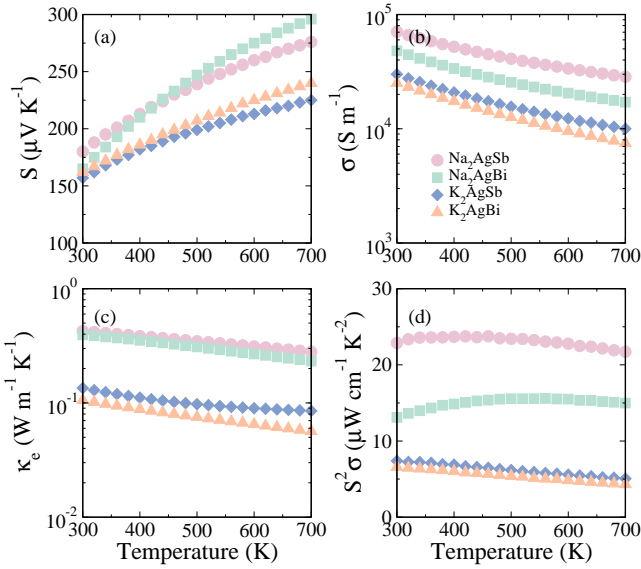


Figure 8. (a) Seebeck coefficient, (b) electrical conductivity, (c) electronic thermal conductivity, and (d) power factor as a function of temperature at optimal carrier concentrations for  $\text{Na}_2\text{AgSb}$  ( $n = 3 \times 10^{20} \text{ cm}^{-3}$ ),  $\text{Na}_2\text{AgBi}$  ( $2 \times 10^{20} \text{ cm}^{-3}$ ),  $\text{K}_2\text{AgSb}$  ( $1 \times 10^{21} \text{ cm}^{-3}$ ), and  $\text{K}_2\text{AgBi}$  ( $4 \times 10^{20} \text{ cm}^{-3}$ ).

higher temperatures, which impacts the carrier mobility, thereby  $\sigma$ .

The electronic thermal conductivity,  $\kappa_e$ , accounts for the contribution of charge carriers to heat transport and are consistent with the electrical conductivity trend, Fig. 8(c).  $\kappa_e$  decreases with temperature, likely due to increased scattering of carriers.  $\text{Na}_2\text{AgSb}$  and  $\text{Na}_2\text{AgBi}$  have higher values of  $\kappa_e$ . In conjunction with Fig. 4, it can be stated that heat propagation through lattice is the dominating mechanism to total thermal conductivity, a typical behavior of semiconductors.

Now coming to the power factor ( $S^2\sigma$ ), which serves as a critical metric for thermoelectric performance, accounting for both  $S$  and  $\sigma$ . As discernible from Fig. 8(d), the power factor begins to plateau near 400 K (450 K) for  $\text{Na}_2\text{AgSb}$  (Bi), followed by a decrease at higher temper-

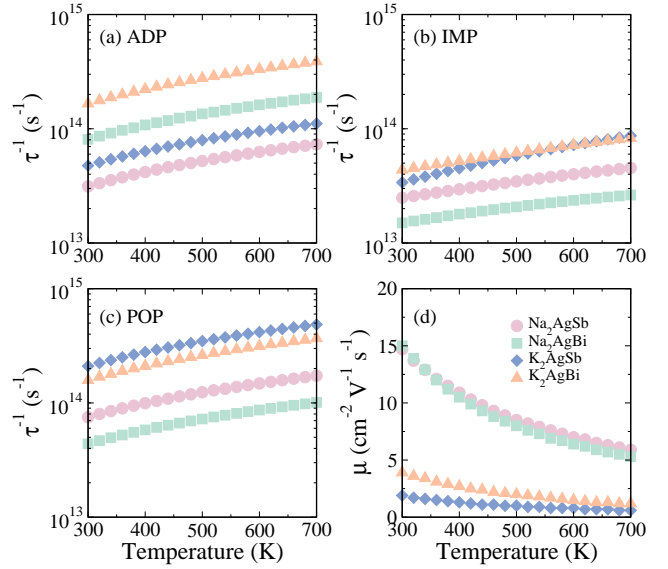


Figure 9. (a), (b), (c) represents the scattering rates for ADP, IMP, POP scattering mechanisms, respectively, and (d) mobility of charge carriers as a function of temperature for optimal carrier concentrations, i.e.,  $\text{Na}_2\text{AgSb}$  ( $n = 3 \times 10^{20} \text{ cm}^{-3}$ ),  $\text{Na}_2\text{AgBi}$  ( $2 \times 10^{20} \text{ cm}^{-3}$ ),  $\text{K}_2\text{AgSb}$  ( $1 \times 10^{21} \text{ cm}^{-3}$ ), and  $\text{K}_2\text{AgBi}$  ( $4 \times 10^{20} \text{ cm}^{-3}$ ).

ature. However, the power factor decreases across the temperature range for  $\text{K}_2\text{AgSb/Bi}$ . We obtained highest power factor for  $\text{Na}_2\text{AgSb}$  across the temperature range, peaking near  $23 \mu\text{W K}^{-1} \text{ cm}^{-2}$  at 420 K.  $\text{Na}_2\text{AgBi}$  follows  $\text{Na}_2\text{AgSb}$ , indicating their superior potential for thermoelectric applications, whereas the power factor for K-based materials ( $\text{K}_2\text{AgSb}$  and  $\text{K}_2\text{AgBi}$ ) are substantially low in comparison to  $\text{Na}_2\text{AgSb/Bi}$ . The possible reason for such a trend could be the dramatic decline in  $\sigma$  values, as noted from Fig. 8(b). To reason out such low  $\sigma$  values in  $\text{K}_2\text{AgSb/Bi}$ , we discuss next the scattering rates and mobility of charge carriers for the optimal carrier concentrations.

We include acoustic deformation potential (ADP), ionized impurity (IMP), and polar optical phonon (POP)

scattering mechanisms to capture the effect of lattice vibrations on charge carriers, the impact of charged impurities on carrier mobility, and interactions between charge carriers and the electric field generated by polar optical phonons, respectively. Fig. 9 illustrates our results of the scattering rates and carrier mobility as a function of temperature for the optimal carrier concentrations. The scattering rates for all mechanisms (ADP, IMP, and POP) increase steadily with temperature, suggesting enhanced interactions of charge carriers with phonons at higher thermal energies. The ADP is the most dominating mechanism for  $\text{Na}_2\text{AgBi}$  and  $\text{K}_2\text{AgBi}$ , whereas the POP mechanism dominates in the case of  $\text{Na}_2\text{AgSb}$  and  $\text{K}_2\text{AgSb}$ . This suggests that the scattering of charge carriers by acoustic phonons is more prominent for Bi-based systems, while charge carriers in Sb-based systems are more prone to scattering through optical phonons. On the other hand, the IMP scattering is least affected by temperature. Overall,  $\text{K}_2\text{AgSb}$  and  $\text{K}_2\text{AgBi}$  depict higher scattering rates in comparison to Na-based counterparts. The mobility trends in Fig. 9(d) reveal a significant reduction with increasing temperature for all systems, driven by the cumulative effect of rising scattering rates. It should be noted that in addition to scattering rates, the mobility of carriers is also dependent on band dispersion and effective mass. Nonetheless,  $\text{Na}_2\text{AgSb}$  and  $\text{Na}_2\text{AgBi}$  maintain comparatively higher mobilities, underscoring their superior charge transport properties under the examined conditions.

The mobility trend mirrors the  $\sigma$  pattern (Fig. 8(b)) and also explains lower  $\sigma$  and power factor values of  $\text{K}_2\text{AgSb}$  and  $\text{K}_2\text{AgBi}$ . Such low mobilities of K-based materials can also be traced to the band dispersions. The bands close to the Fermi level in the valence band region are relatively flat for  $\text{K}_2\text{AgSb/Bi}$  in comparison to  $\text{Na}_2\text{AgSb/Bi}$ , Fig. 1. This analysis highlights the critical influence of scattering mechanisms and carrier concentration optimization on the transport properties of proposed thermoelectric materials, offering valuable insights for achieving high-performance thermoelectric efficiency.

#### IV. DISCUSSION

Our theoretical predictions suggest exceptionally good high temperature thermoelectric performance for the investigated materials, especially  $\text{Na}_2\text{AgSb}$  and  $\text{Na}_2\text{AgBi}$ . However, the theoretical prediction of exotic properties should meet the experimental realization, which is subject to various challenges. As these materials (except  $\text{Na}_2\text{AgBi}$ ) are already synthesized, the material fabrication should not be deemed a major concern. However, achieving the proposed optimal carrier concentrations could be the prime obstacle in meeting the desired figure of merit. Two prominent ways of controlling the carrier concentration are extrinsic doping or tuning the intrinsic defects.  $\text{Yb}_{14}\text{Mn}_{1-x}\text{Al}_x\text{Sb}_{11}$  [78] and  $\text{Ca}_x\text{Yb}_{1-x}\text{Zn}_2\text{Sb}_2$  [79] are examples of some well-known extrinsic  $p$ -type

Zintl phases, offering the feasibility of creating the extrinsic compositions. In light of such evidence, group-IV elements (like Si, Ge, Sn) in place of Sb/Bi or group-III elements (e.g., Al, Ga) in place of Ag could be the most favorable choices for achieving extrinsic  $p$ -type materials. On the other hand, the Zintl phases are also found to have intrinsic  $p$ -type compositions. For instance, Toberer *et al.* [80] synthesized  $p$ -type  $\text{LiZnSb}$  samples, with a carrier concentration of the order of  $10^{20}$  carriers  $\text{cm}^{-3}$ . In the case of  $\text{Na}_2\text{AgSb/Bi}$  and  $\text{K}_2\text{AgSb/Bi}$ , the loss of Na/K ions to oxidation during synthesis could result in intrinsic  $p$ -type materials. The absence of four Na/K ions will correspond to 0.04 carriers per formula unit, which is approximately of the order of  $10^{20}$  carriers  $\text{cm}^{-3}$ . Such doping levels are also equivalent to our proposed carrier concentrations, suggesting their experimental realization. In addition, the credibility of computational methods used for predicting materials' properties is also of key importance.

In this study, we have used state-of-the-art computational techniques which are well tested with experimental works for a wide range of materials [52, 81–84]. However, we have not taken into account the anharmonic phonon renormalization due to computationally expensive requirements. We are of the opinion that it will be important to qualitatively discuss the impact of anharmonic phonon renormalization on our predicted results. It has been found in various studies that anharmonic phonon renormalization impacts more the low frequency phonons [85, 86]. This suggests stronger anharmonicity in the low frequency phonons, suggesting increased acoustic-optical phonons interactions. This could eventually lead to four-phonon scattering mechanism, which is found to further diminish the lattice thermal conductivity. Studies have found that four-phonon processes are more impactful at high temperatures and frequencies [62–64]. Our calculated P3-phase space further suggests three-phonon scattering mechanism as more influential in low frequency region, i.e., less than 2 THz. As low frequency acoustic modes are major contributors to heat conduction, it can be surmised that four-phonon processes are likely to lower the lattice thermal conductivity at higher frequencies and temperatures.

Nevertheless, our results show the importance of chemical composition and optimal carrier concentrations in optimizing thermoelectric properties. The better performance of Na-based systems suggests that light alkali metal cations, combined with Ag-Bi/Sb frameworks, could be effective in achieving high thermoelectric efficiency. Furthermore, the differences between Na- and K-based systems highlight the tunability of transport properties through cation substitution. This could pave the way for material design for specific operating conditions. The promising performance of  $\text{Na}_2\text{AgSb}$  and  $\text{Na}_2\text{AgBi}$  warrants further experimental validation and exploration of strategies to achieve the optimal carrier concentrations. Additionally, the role of phonon scattering mechanisms in suppressing lattice thermal conductivity in these

compounds should be investigated using advanced techniques such as anharmonic phonon calculations.

## V. SUMMARY

In conclusion, we studied the alkali metal-based family of Zintl phases  $X_2AgY$  ( $X = Na, K$ ;  $Y = Sb, Bi$ ) using density functional theory based first-principles simulations and by solving Boltzmann transport equations. The Na- and K-based materials crystallize in orthorhombic  $Cmcm$  and  $C222_1$  symmetry, respectively. All materials are semiconducting, possessing band gap in the range of 0.8-1.8 eV, sufficient to avoid any bipolar conduction. The dynamical stability of the systems is ascertained by phonon dispersions. The main highlight of the work is the remarkably low lattice thermal conductivity values ( $< 1 \text{ W m}^{-1} \text{ K}^{-1}$ ), comparable to benchmark thermoelectric materials such as SnSe, PbTe, and  $Bi_2Te_3$ . It is found that around 80% contribution to thermal conductivity comes from acoustic and low-lying optical modes. We ascribed low thermal conductivity values to low phonon velocities, short lifetimes, and large scattering phase space. Notably, an avoided crossing in the

phonon spectrum, indicative of rattling behavior, was observed in all systems except  $Na_2AgSb$ . The rattling phenomenon is associated with suppressing the dispersion of acoustic modes, which could lead to low phonon velocities. In addition, in K-based materials, a gap in optical modes is found, which often results in the flattening of phonon modes. Furthermore, the observed bonding heterogeneity also accounts for their low thermal conductivity. Combining these properties with electrical transport, we determined a high figure of merit at 700 K, i.e.,  $ZT \sim 2.1$  for  $Na_2AgSb$ , 1.7 for  $Na_2AgBi$ , 0.9 for  $K_2AgSb$ , and 1.0 for  $K_2AgBi$ . Our study underscores the importance of chemical composition and carrier engineering in optimizing thermoelectric materials.

## ACKNOWLEDGMENTS

M. Z. is thankful to SERB-DST (File No. PDF/2022/002559) for the financial assistance. B. K. M. acknowledges the funding support from the SERB, DST (ECR/2016/001454). The calculations are performed using the High Performance Computing cluster, Padum, at the Indian Institute of Technology Delhi.

- 
- [1] M. A. Zoui, S. Bentouba, J. G. Stocholm, and M. Bourouis, *Energies* **13**, 3606 (2020).
- [2] M. Hamid Elsheikh, D. A. Shnawah, M. F. M. Sabri, S. B. M. Said, M. Haji Hassan, M. B. Ali Bashir, and M. Mohamad, *Renew. Sustain. Energy Rev.* **30**, 337 (2014).
- [3] V. S. Arutyunov and G. V. Lisichkin, *Russ. Chem. Rev.* **86**, 777 (2017).
- [4] C. Forman, I. K. Muritala, R. Pardemann, and B. Meyer, *Renew. Sustain. Energy Rev.* **57**, 1568 (2016).
- [5] G. Zhang, Q. Yu, and X. Li, *Dalton Trans.* **39**, 993 (2010).
- [6] R. B. Jackson, P. Friedlingstein, C. L. Quéré, S. Abernethy, R. M. Andrew, J. G. Canadell, P. Ciais, S. J. Davis, Z. Deng, Z. Liu, J. I. Korsbakken, and G. P. Peters, *Environ. Res. Lett.* **17**, 031001 (2022).
- [7] S. Liu, V. P. Biju, Y. Qi, W. Chen, and Z. Liu, *NPG Asia Mater.* **15**, 27 (2023).
- [8] A. Züttel, *Mater. Today* **6**, 24 (2003).
- [9] T.-Z. Ang, M. Salem, M. Kamarol, H. S. Das, M. A. Nazari, and N. Prabaharan, *Environ. Res. Lett.* **43**, 100939 (2022).
- [10] R. Singh, S. Dogra, S. Dixit, N. I. Vatin, R. Bhardwaj, A. K. Sundramoorthy, H. Perera, S. P. Patole, R. K. Mishra, and S. Arya, *Hybr. Adv.* **5**, 100176 (2024).
- [11] Z. Wehbi, R. Taher, J. Faraj, C. Castelain, and M. Khaled, *Energy Rep.* **8**, 1361 (2022), technologies and Materials for Renewable Energy, Environment and Sustainability.
- [12] F. Garmroudi, A. Riss, M. Parzer, N. Reumann, H. Müller, E. Bauer, S. Khmelevskiy, R. Podloucky, T. Mori, K. Tobita, Y. Katsura, and K. Kimura, *Phys. Rev. B* **103**, 085202 (2021).
- [13] S. Karmakar and T. Saha-Dasgupta, *Phys. Rev. Materials* **4**, 124007 (2020).
- [14] J. Maassen, *Phys. Rev. B* **104**, 184301 (2021).
- [15] T. Berry, C. Fu, G. Auffermann, G. H. Fecher, W. Schnelle, F. Serrano-Sanchez, Y. Yue, H. Liang, and C. Felser, *Chem. Mater.* **29**, 7042 (2017).
- [16] S. R. Boona, *Nature* **549**, 169 (2017).
- [17] Y. K. Lee, K. Ahn, J. Cha, C. Zhou, H. S. Kim, G. Choi, S. I. Chae, J.-H. Park, S.-P. Cho, S. H. Park, Y.-E. Sung, W. B. Lee, T. Hyeon, and I. Chung, *J. Am. Chem. Soc.* **139**, 10887 (2017).
- [18] L. E. Bell, *Science* **321**, 1457 (2008).
- [19] M. Zeeshan, T. Nautiyal, J. van den Brink, and H. C. Kandpal, *Phys. Rev. Mater.* **2**, 065407 (2018).
- [20] L. Xi, J. Yang, L. Wu, J. Yang, and W. Zhang, *J. Materiom.* **2**, 114 (2016).
- [21] J. Wei, H. J. Liu, L. Cheng, J. Zhang, J. H. Liang, P. H. Jiang, D. D. Fan, and J. Shi, *AIP Adv.* **5**, 107230 (2015).
- [22] X.-Y. Xin, J. Ma, H.-Q. Liu, Y.-J. Gu, Y.-F. Wang, and H.-Z. Cui, *J. Mater. Sci. Technol.* **151**, 66 (2023).
- [23] G. J. Snyder and E. S. Toberer, *Nature Materials* **7**, 105 (2008).
- [24] S. Chen and Z. Ren, *Materials Today* **16**, 387 (2013).
- [25] A. Mehdizadeh Dehkordi, M. Zebarjadi, J. He, and T. M. Tritt, *Mater. Sci. Eng. R: Rep.* **97**, 1 (2015).
- [26] C. K. Vishwakarma, M. Zeeshan, and B. K. Mani, *J. Phys. Chem. C* **128**, 2311 (2024).
- [27] M. Dutta, S. Matteppanavar, M. V. D. Prasad, A. Pandey, A. Warankar, P. Mandal, A. Soni, U. V. Waghmare, and K. Biswas,

- J. Am. Chem. Soc. **141**, 20293 (2019).
- [28] M. K. Jana, K. Pal, U. V. Waghmare, and K. Biswas, *Angew. Chem. Int. Ed.* **55**, 7792 (2016).
- [29] C. Chen, Z. Feng, H. Yao, F. Cao, B.-H. Lei, Y. Wang, Y. Chen, D. J. Singh, and Q. Zhang, *Nature Commun.* **12**, 5718 (2021).
- [30] P. Qiu, X. Shi, and L. Chen, *Energy Storage Mater.* **3**, 85 (2016).
- [31] X. Li, P.-F. Liu, E. Zhao, Z. Zhang, T. Guidi, M. D. Le, M. Avdeev, K. Ikeda, T. Otomo, M. Kofu, K. Nakajima, J. Chen, L. He, Y. Ren, X.-L. Wang, B.-T. Wang, Z. Ren, H. Zhao, and F. Wang, *Nature Commun.* **11**, 942 (2020).
- [32] G. A. Slack, in *CRC Handbook of Thermoelectrics*, edited by D. M. Rowe (CRC Press, Boca Raton, FL, 1995) pp. 407–440.
- [33] J. Wang, M. Guo, J. Zhu, D. Qin, F. Guo, Q. Zhang, W. Cai, and J. Sui, *J. Mater. Sci. Technol.* **59**, 189 (2020).
- [34] A. Balvanz, J. Qu, S. Baranets, E. Ertekin, P. Gorai, and S. Bobev, *Chem. Mater.* **32**, 10697 (2020).
- [35] C. Chen, W. Xue, S. Li, Z. Zhang, X. Li, X. Wang, Y. Liu, J. Sui, X. Liu, F. Cao, Z. Ren, C.-W. Chu, Y. Wang, and Q. Zhang, *Proc. Natl. Acad. Sci. U.S.A.* **116**, 2831 (2019).
- [36] J. H. Roudebush, J. Grebenkemper, Y. Hu, N. Kazem, M. Abdusalyamova, and S. M. Kauzlarich, *J. Solid State Chem.* **211**, 206 (2014).
- [37] E. S. Toberer, A. Zevalkink, N. Crisosto, and G. J. Snyder, *Adv. Funct. Mater.* **20**, 4375 (2010).
- [38] A. Zevalkink, G. Pomrehn, Y. Takagiwa, J. Swallow, and G. J. Snyder, *ChemSusChem* **6**, 2316 (2013).
- [39] S. Zheng, K. Peng, S. Xiao, Z. Zhou, X. Lu, G. Han, B. Zhang, G. Wang, and X. Zhou, *J. Adv. Ceram.* **11**, 1604 (2022).
- [40] S. M. Kauzlarich, *Chem. Mater.* **35**, 7355 (2023).
- [41] K. Pal, J. He, and C. Wolverton, *Chem. Mater.* **30**, 7760 (2018).
- [42] S.-F. Wang, J.-R. Zhang, and F.-W. Wang, *Phys. Rev. B* **108**, 235213 (2023).
- [43] C. Wei, Z. Feng, Y. Yan, G. Zhao, Y. Fu, and D. J. Singh, *Phys. Rev. B* **108**, 235203 (2023).
- [44] G. Kresse and J. Furthmüller, *Comput. Mater. Sci.* **6**, 15 (1996).
- [45] G. Kresse and J. Furthmüller, *Phys. Rev. B* **54**, 11169 (1996).
- [46] J. P. Perdew, K. Burke, and M. Ernzerhof, *Phys. Rev. Lett.* **77**, 3865 (1996).
- [47] F. Tran and P. Blaha, *Phys. Rev. Lett.* **102**, 226401 (2009).
- [48] O. Jepsen and O. K. Andersen, (1999).
- [49] A. M. Ganose, J. Park, A. Faghaninia, R. Woods-Robinson, K. A. Persson, and A. Jain, *Nature Commun.* **12**, 2222 (2021).
- [50] A. Matthiessen and C. Vogt, *Annalen der Physik* **198**, 19 (1864).
- [51] P. A. M. Dirac and N. H. D. Bohr, *Proc. R. Soc. A* **114**, 243 (1927).
- [52] A. Togo and I. Tanaka, *Scr. Mater.* **108**, 1 (2015).
- [53] A. Togo, L. Chaput, and I. Tanaka, *Phys. Rev. B* **91**, 094306 (2015).
- [54] W. Li, J. Carrete, N. A. Katcho, and N. Mingo, *Comp. Phys. Commun.* **185**, 1747–1758 (2014).
- [55] H.-U. Schuster, C. Mues, and W. Jung, *Z. Naturforsch. B* **34**, 354 (1979).
- [56] H.-C. Wang, S. Botti, and M. A. L. Marques, *npj Comput. Mater.* **7**, 12 (2021).
- [57] G. Savelsberg and H. Schäfer, *Z. Naturforsch. B* **32**, 745 (1977).
- [58] See Supplemental Material at [URL] for Wyckoff Positions, electronic structure with PBE and mBJ, transport properties, and convergence tests..
- [59] R. Nesper, *Z. Anorg. Allg. Chem.* **640**, 2639 (2014).
- [60] L. H. Rodriguez, K. B. Spooner, M. Einhorn, and D. O. Scanlon, *J. Mater. Chem. C* **11**, 9124 (2023).
- [61] H. Lin, G. Tan, J.-N. Shen, S. Hao, L.-M. Wu, N. Caltà, C. Malliakas, S. Wang, C. Uher, C. Wolverton, and M. G. Kanatzidis, *Angew. Chem. Int. Ed.* **55**, 11431 (2016).
- [62] T. Feng, L. Lindsay, and X. Ruan, *Phys. Rev. B* **96**, 161201 (2017).
- [63] Y. Xia, *App. Phys. Lett.* **113**, 073901 (2018).
- [64] T. Yue, Y. Zhao, J. Ni, S. Meng, and Z. Dai, *Phys. Rev. B* **107**, 024301 (2023).
- [65] L.-D. Zhao, S.-H. Lo, Y. Zhang, H. Sun, G. Tan, C. Uher, C. Wolverton, V. P. Dravid, and M. G. Kanatzidis, *Nature* **508**, 373 (2014).
- [66] D. Bessas, I. Sergueev, H.-C. Wille, J. Perbon, D. Ebling, and R. P. Hermann, *Phys. Rev. B* **86**, 224301 (2012).
- [67] H. Wang, Y. Pei, A. D. LaLonde, and G. J. Snyder, *Adv. Mater.* **23**, 1366 (2011).
- [68] R. Guo, X. Wang, Y. Kuang, and B. Huang, *Phys. Rev. B* **92**, 115202 (2015).
- [69] S. R. Brown, S. M. Kauzlarich, F. Gascoin, and G. J. Snyder, *Chem. Mater.* **18**, 1873 (2006).
- [70] X.-J. Wang, M.-B. Tang, J.-T. Zhao, H.-H. Chen, and X.-X. Yang, *App. Phys. Lett.* **90**, 232107 (2007).
- [71] H. Tamaki, H. K. Sato, and T. Kanno, *Adv. Mater.* **28**, 10182 (2016).
- [72] L. Borgsmiller, Q. Li, M. Y. Toriyama, and G. J. Snyder, *Adv. Energy Mater.* **13**, 2300393 (2023).
- [73] K. Guo, Y. Zhang, S. Yuan, Q. Tang, C. Lin, P. Luo, J. Yang, S. Pan, L.-D. Zhao, G. Cheng, J. Zhang, and J. Luo, *Angew. Chem. Int. Ed.* **62**, e202212515 (2023).
- [74] H. Zhu, R. He, J. Mao, Q. Zhu, C. Li, J. Sun, W. Ren, Y. Wang, Z. Liu, Z. Tang, A. Sotnikov, Z. Wang, D. Broido, D. J. Singh, G. Chen, K. Nielsch, and Z. Ren, *Nature Commun.* **9**, 2497 (2018).
- [75] H. Zhu, J. Mao, Y. Li, J. Sun, Y. Wang, Q. Zhu, G. Li, Q. Song, J. Zhou, Y. Fu, R. He, T. Tong, Z. Liu, W. Ren, L. You, Z. Wang, J. Luo, A. Sotnikov, J. Bao, K. Nielsch, G. Chen, D. J. Singh, and Z. Ren, *Nature Commun.* **10**, 270 (2019).
- [76] X. Pang, M. He, F. Zhang, B. Jia, W. Wang, X. Cao, M. Song, X. Chao, Z. Yang, and D. Wu, *Chem. Eng. J.* **481**, 148457 (2024).
- [77] G. Tan, F. Shi, S. Hao, L.-D. Zhao, H. Chi, X. Zhang, C. Uher, C. Wolverton, V. P. Dravid, and M. G. Kanatzidis, *Nature Commun.* **7**, 12167 (2016).
- [78] C. A. Cox, E. S. Toberer, A. A. Levchenko, S. R. Brown, G. J. Snyder, A. Navrotsky, and S. M. Kauzlarich, *Chem. Mater.* **21**, 1354 (2009).
- [79] F. Gascoin, S. Ottensmann, D. Stark, S. Haile, and G. Snyder, *Adv. Funct. Mater.* **15**, 1860 (2005).
- [80] E. S. Toberer, A. F. May, C. J. Scanlon, and G. J. Snyder, *J. App. Phys.* **105**, 063701 (2009).
- [81] J. M. Skelton, S. C. Parker, A. Togo, I. Tanaka, and A. Walsh, *Phys. Rev. B* **89**, 205203 (2014).

- [82] J. Rundle and S. Leoni, *J. Phys. Chem. C* **126**, 14036 (2022).
- [83] J. M. Flitcroft, I. Pallikara, and J. M. Skelton, *Solids* **3**, 155 (2022).
- [84] W. Dou, K. B. Spooner, S. R. Kavanagh, M. Zhou, and D. O. Scanlon, *J. Am. Chem. Soc.* **146**, 17679 (2024).
- [85] Z. Yao, W. Cao, Z. Wang, L. Miao, J. Shi, and R. Xiong, *Phys. Chem. Chem. Phys.* **25**, 26236 (2023).
- [86] D. Guo, Z. Xu, H. Zhang, C. Li, J. Sun, X. Luo, and Y. Ma, *J. Alloys Compd.* **932**, 167525 (2023).